JM PAPERS

Inertial collapse of a gas bubble in a shear flow near a rigid wall

Sahil Bhola[1],[†], Mauro Rodriguez Jr.[2], Shahaboddin A. Beig[3], Charlotte N. Barbier[4] and Eric Johnsen[3]

[1]Department of Aerospace Engineering, University of Michigan, Ann Arbor, MI 48109 USA

[2]School of Engineering, Brown University, Providence, RI 02912 USA

[3]Department of Mechanical Engineering, University of Michigan, Ann Arbor, MI 48109 USA

[4]Oak Ridge National Laboratory, Oak Ridge, TN 37830 USA

Despite the extensive research on bubble collapse near rigid walls, the bubble collapse dynamics in the presence of shear flow near a rigid wall is poorly understood. We conduct direct simulations of the Navier–Stokes equations to explore the bubble dynamics and pressures during bubble collapse near a rigid, flat wall under linear shear flow conditions. We examine the dependence of the bubble collapse morphology and wall pressures on the initial bubble location and shear rate. We find that shear distorts the bubble, generating two re-entrant jets – one developing from the side opposite to the mean flow and the other from the far end toward the wall. Upon impact of the jet on the opposite side of the bubble, water-hammer shocks are produced, which propagate outward and interact with the convoluted bubble shape. The shock stretches the bubble towards the wall, resulting in a closer impact location for the jet originating from the far end compared with the case with no shear flow. The water-hammer pressure location can be approximated as the theoretical distance travelled by a particle initialised at the bubble centre with the corresponding constant shear flow velocity. The maximum wall pressures can thus be predicted by considering the distance between the far jet impingement location and the wall along the wall-normal direction. As the shear rate is increased, the maximum wall pressure increases, although only marginally. We determine the critical initial stand-off distance from the wall at which the bubble morphology is shear dominated, i.e. characterised by converging re-entrant jets.

Key words: bubble dynamics, cavitation

† Email address for correspondence: sbhola@umich.edu

S. Bhola, M. Rodriguez Jr., S.A. Beig, C.N. Barbier and E. Johnsen

1. Introduction

Cavitation erosion is prevalent in applications such as fuel injectors, propellers, therapeutic ultrasound and ultrasonic cleaning. In hydrodynamic applications, cavitation-induced pitting damages solid surfaces and may constitute a lifetime-limiting factor (Blake & Gibson 1987). For example, cavitation erosion poses design constraints on the mercury target vessel and proton-beam power limitations in the Spallation Neutron Source (Haines *et al.* 2014; Riemer *et al.* 2014; Winder, Lin & Mach 2021). Applications such as diesel injector nozzles (Chaves *et al.* 1995; Gavaises *et al.* 2007; Giannadakis, Gavaises & Arcoumanis 2008), hydraulic turbines (Escaler *et al.* 2006; Brijkishore, Khare & Prasad 2021) and hydrofoils (Patella, Archer & Flageul 2012; Venning, Pearce & Brandner 2022) have also observed degradation in performance due to cavitation erosion. In some cases, the cavitating bubble can form near a solid boundary within the boundary layer or may be submerged in a mean shear flow. For example, in ultrasonic cleaning applications, the ultrasonic waves can result in acoustic streaming, which results in travelling cavitation bubbles that can remove contaminants with a greater efficiency (Kim *et al.* 2009; Shchukin *et al.* 2011; Kim *et al.* 2014; Ando, Sugawara & Sakota 2021). Ceccio & Brennen (1991) and De Chizelle, Ceccio & Brennen (1995) experimentally observed travelling cavitation bubbles over standard head forms where hemispherical cavitation bubbles deform into wedge-like shapes due to the interaction of the bubbles with the flow, which shears the bubble and fragments it into smaller bubbles, resulting in multiple collapses. These additional albeit weaker collapses generate noise and extent of damage to the surface. Dular *et al.* (2019) examined a single bubble collapsing near a surface in a homogeneous velocity field ($5 \, \mathrm{m \, s^{-1}}$) parallel to the adjacent surface. The shear flow deflects the re-entrant jet in the shear flow direction, resulting in an asymmetric splash of the collapsing bubble onto the neighbouring wall. The deflected re-entrant jet was reported to be the primary damage mechanism for a bubble initially detached and located a finite distance from the wall.

The collapse of a bubble is the central problem of cavitation erosion. Rayleigh (1917) demonstrated that a spherical cavity imploding in an infinite, initially stationary fluid produces high pressures in the liquid. Upon collapse, energy is released as a shock propagating radially outward, which can damage neighbouring materials (Plesset 1949). The shock produced at collapse plays an essential role in cavitation erosion (Hickling & Plesset 1964). Early experiments showed that the presence of a wall leads to asymmetry, resulting in an axisymmetric collapse (Naudé & Ellis 1961; Benjamin & Ellis 1966; Gibson 1968). During the collapse, the bubble migrates towards the wall due to the attraction from the image bubble. The axisymmetric collapse is characterised by the formation of a re-entrant jet directed towards the wall. This jet originates from the bubble interface furthest from the wall, penetrates the bubble, accelerates up to several hundred metres and impinges on the opposite bubble side (Plesset & Chapman 1971; Lauterborn & Bolle 1975; Philipp & Lauterborn 1998). Jet impingement produces an outward propagating shock. Soon after the production of this water-hammer shock, the bubble continues imploding, reaches minimum volume and produces an implosion shock (Supponen *et al.* 2017). If the bubble is sufficiently close to the wall, then it may directly impinge upon the wall. However, experimental efforts to relate material damage to the shock pressure and jet impingement on the wall via experiments or theory have proven to be challenging due to the presence of a wide range of spatio-temporal scales (Hickling & Plesset 1964; Shutler & Mesler 1965; Gonzalez-Avila, Denner & Ohl 2021).

Numerical simulations have provided further insights into the bubble collapse near a wall. Early studies used potential flow to examine the re-entrant jet formation (Benjamin & Ellis 1966; Plesset & Chapman 1971). The shape evolution and re-entrant

jet velocity results agreed well with experimental observations made by Benjamin & Ellis (1966) and Lauterborn & Bolle (1975). However, these methods consider the liquid to be incompressible and, therefore, are unable to capture the shocks produced during the collapse and their interaction with the nearby rigid wall. Johnsen & Colonius (2009) numerically solved the Euler equations with a finite-volume method using an interface-capturing approach and achieved good agreement with the experimental collapse time (Lindau & Lauterborn 2003) and wall pressure (Shima, Tomita & Takahashi 1984) for different initial stand-off distances. Beig (2018) examined the collapse morphology, dynamics and maximum wall pressures produced by the axisymmetric collapse at various initial stand-off distances. The work showed that the driving pressure across the bubble interface and initial stand-off distance from the rigid boundary determine the bubble collapse time and morphology of the re-entrant jet, respectively. Results agreed with the experimental bubble shape evolution (Philipp & Lauterborn 1998), re-entrant jet speed (Brujan *et al.* 2002; Supponen *et al.* 2016) and maximum pressure decay (Cole 1948). These methods have also been used to study the bubble collapse dynamics and pressures at surfaces near a vessel (Coralic & Colonius 2013), corner (White, Beig & Johnsen 2023) and crevice (Trummler *et al.* 2020).

A limited number of numerical investigations have been conducted on the cavitation dynamics in a shear flow. Two distinct bubble collapse morphologies are observed in simulations: (i) re-entrant jet deflection, also observed experimentally by Dular *et al.* (2019), and (ii) shear-induced converging jets. Yu, Ceccio & Tryggvason (1995) numerically simulated a bubble collapse in a shear flow at a driving pressure of 50 kPa to investigate interactions with the boundary layer. As the shear rate increases, the re-entrant jet becomes smaller, and the jet impact location moves further downstream in the flow direction. Additionally, as the shear flow velocity approaches the characteristic re-entrant jet speed, the bubble collapse rate increases and approaches the inviscid, no-shear limit. Dabiri, Sirignano & Joseph (2010) and Chen (2010) considered bubble collapse in a flow generated by two shearing plates and observed the bubble deforming into an ellipsoid shape. High-pressure regions near the major axis of the ellipsoid were observed, followed by the emergence of a concave shape on the surface of the bubble. Dabiri *et al.* (2010) reported the formation of re-entrant jets along the minor axis of the ellipsoid, which impact the bubble interface, resulting in vapour entrapment and the formation of 'satellite bubbles'. Although these studies examined the effect of initial shear rates and stand-off distances on the bubble shape morphology, these simulations could not represent shock wave generation and propagation, as they consider semi-incompressible fluid flow with only the gas being compressible.

This work aims to investigate the competing effect between inertia and shear on the collapse of a gas bubble in a shear flow near a rigid wall. By varying the initial shear rate and stand-off distance from the wall in our numerical simulations, we examine the bubble morphologies and characterise the outward-propagating shock impingement on the nearby wall and the resulting maximum wall pressure at the wall. The manuscript is organised as follows. In § 2, the problem set-up is presented. The governing equations and numerical solver are then discussed. In § 3, we compare the bubble collapse dynamics and maximum wall pressures for different shear rates and stand-off distances. We provide our conclusions in § 4.

2. Problem set-up and governing equations

Figure 1 illustrates our problem set-up. We consider a linear shear flow near an infinitely long, flat rigid wall with an initially spherical gas bubble of radius R_o surrounded by
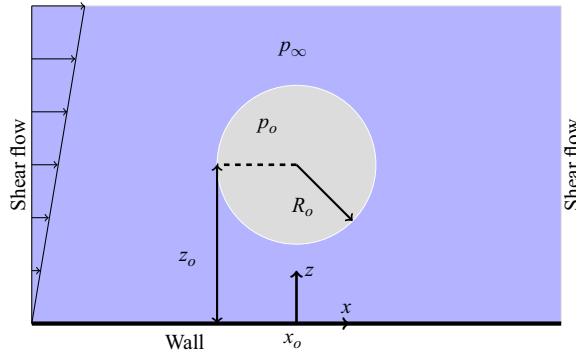
Figure 1. Schematic of an initially spherical gas bubble of radius R_o in a shear flow located at a distance z_o away form a rigid, flat wall. The y-axis direction points out of the page and x_o is the wall centreline location, $x = 0$.

water of density ρ_l, pressure p_∞ and temperature T_∞ and placed at a distance of z_o from the wall. In practical applications, bubbles can grow from $O(1)$ to $O(10^2)\,\mu$m, resulting in a non-spherical shape and non-uniform pressure distribution due to the presence of the rigid wall and shear (Dabiri *et al.* 2010; Tiwari, Pantano & Freund 2015; Dular *et al.* 2019; Gonzalez-Avila *et al.* 2021). To study the effect of shear and distance from the wall solely on the bubble collapse dynamics, we initialise with an initial radius $R_o = 500\,\mu$m for all the cases. Thus comparing similar bubble collapses. This initially spherical gas bubble has an equivalent volume to the bubbles after growth, thus considering the equivalent volume after vapour condensation and ignoring surface tension effects (Lauterborn *et al.* 2018; Gonzalez-Avila *et al.* 2021). Bubbles of similar radius have been studied experimentally (Dular *et al.* 2019; Gonzalez-Avila *et al.* 2021) and numerically investigated (Yu *et al.* 1995; Beig, Aboulhasanzadeh & Johnsen 2018; Bußmann *et al.* 2023). The initial non-dimensional stand-off distance is $\gamma_o = z_o/R_o$. The bubble contains vapour, which is modelled as a non-condensable ideal gas with pressure $p_o = 3550\,$Pa and temperature $T_o = 300\,$K. The initial liquid pressure $p_\infty = 5\,$MPa is considered, motivated by the studies of Franc *et al.* (2011), who identify it as relevant for cavitation erosion applications; we define $\Delta p = p_\infty - p_o$. The shear across the bubble is $\dot{\varsigma}_o = ((u_x)_{\gamma_o+1} - (u_x)_{\gamma_o-1})/2R_o$, where $(u_x)_{\gamma_o+1}$ and $(u_x)_{\gamma_o-1}$ are the x-components of the velocity at the top of the bubble (farthest from the wall) and bottom of the bubble (closest to the wall), respectively. A symmetry boundary condition is used along the xz-centreplane. The slip non-reflecting boundary conditions of Thompson (1990) are used at the top boundary to enforce the top plate velocity corresponding to the desired shear rate. A perfectly reflecting, no-slip boundary condition represents the rigid wall. The left, right and back boundaries are non-reflective boundary conditions. The computational domain has size $8R_o \times 4R_o \times 6R_o$. Beig (2018) showed that 128 computational cells per initial bubble radius can resolve the maximum wall pressure due to inertia-driven collapse. Previous studies (Yu *et al.* 1995; Dabiri *et al.* 2010; Dular *et al.* 2019) have shown that bubble collapse under shear flow results in a larger bubble surface area and, therefore, in the present study, 128 cells per initial bubble radius is considered sufficient resolution.

We perform direct simulations of the Navier–Stokes equations with the five-equation multiphase model (Kapila *et al.* 2001), where pressure and velocity equilibria between the phases are assumed. This model and its improvements have been widely applied to study a range of phenomena (Allaire, Clerc & Kokh 2002; Murrone & Guillard 2005; Perigaud

& Saurel 2005; Petitpas *et al.* 2009; Beig 2018; Yang *et al.* 2021; Rodriguez *et al.* 2022; Bidi *et al.* 2023; Yang *et al.* 2023). We solve the mass conservation, momentum and energy balance equations in the absence of gravity

$$\frac{\partial \rho}{\partial t} + \frac{\partial}{\partial x_j}(\rho u_j) = 0, \tag{2.1a}$$

$$\frac{\partial}{\partial t}(\rho^{(1)}\alpha^{(1)}) + \frac{\partial}{\partial x_j}(\rho^{(1)}\alpha^{(1)}u_j) = 0, \tag{2.1b}$$

$$\frac{\partial}{\partial t}(\rho u_i) + \frac{\partial}{\partial x_j}(\rho u_i u_j + p\delta_{ij}) = \frac{\partial \tau_{ij}}{\partial x_j}, \tag{2.1c}$$

$$\frac{\partial E}{\partial t} + \frac{\partial}{\partial x_j}((E + p)u_j) = \frac{\partial}{\partial x_k}(u_i \tau_{ik} - Q_k), \tag{2.1d}$$

where ρ is the total (mixture) density, u_i the velocity vector, Q_k the heat flux, $\alpha^{(1)}$ the volume fraction of water and we use indices $i, j = 1, 2$ and 3; repeated indices denote summation. Equation (2.1b) is the mass conservation equation for the water component. The total energy per unit volume E comprises internal and kinetic contributions: $E = \rho e + \frac{1}{2}\rho u_k^2$. An additional species transport equation is solved for $\alpha^{(k)}$ in non-conservative form to maintain interfacial equilibrium conditions for velocity, pressure and temperature (Beig & Johnsen 2015).

The Noble–Abel stiffened-gas equation of state of Le Métayer & Saurel (2016) is used to relate the internal energy to pressure

$$\rho(e - q) = \frac{p(1 - \rho b)}{n - 1} + \frac{nB(1 - \rho b)}{n - 1}, \tag{2.2}$$

where q, n, B and b are material constants prescribed to produce the correct propagation speeds in water. Table 1 lists the properties of liquid water and water vapour. Fourier conduction describes the heat diffusion process: $Q_i = -\kappa \partial T/\partial x_i$, where κ is the thermal conductivity. Fluids behave in a Newtonian fashion, such that the viscous stress is given by $\tau_{ij} = \mu_b \dot{\epsilon}_{kk} \delta_{ij} + \mu_s \dot{\epsilon}_{ij}^{(d)}$, where μ_b is the bulk viscosity, μ_s the shear viscosity and $\dot{\epsilon}_{ij}$ the strain-rate tensor with $\dot{\epsilon}_{ij}^{(d)}$ as its deviatoric part. For water vapour, $\kappa = 0.02\,\text{W}\,(\text{m}\,\text{K})^{-1}$ and $\mu_b = \mu_s = 10^{-5}\,\text{Pa}\,\text{s}$; for liquid water, $\kappa = 0.6\,\text{W}\,(\text{m}\,\text{K})^{-1}$ and $\mu_b = \mu_s = 9 \times 10^{-4}\,\text{Pa}\,\text{s}$. Based on the characteristic speed $u_c = \sqrt{\Delta p/\rho_l}$ defined by Plesset & Chapman (1971) and R_o, the Reynolds number is of $O(10^4)$ such that the flow is inertia driven and the bulk viscosity would have negligible effects. Thus, bulk viscosity is assumed to be identical to the shear viscosity for numerical convenience. For the characteristic speed and R_o, the estimated Weber number is 3.4×10^4. Using the shear velocity at the top domain boundary, the Weber numbers range between 1.9×10^4 and 3×10^5. For such large Weber numbers, surface tension has negligible influence and, therefore, can be neglected. Since the bubble collapses under consideration are inertia or shear dominated, mass transfer (Beig 2018) and phase change (Storey & Szeri 2000; Preston 2004) can be neglected. We use the numerical approach presented by Beig & Johnsen (2015) to solve the resulting set of equations.

Three non-dimensional parameters govern the problem: the initial driving pressure $p_\infty/\rho_l a_l(\Delta p/\rho_l)^{1/2}$, stand-off distance $\gamma_o = z_o/R_o$ and shear rate $\omega_o = 2\dot{\varsigma}_o R_o/u_c$. Our focus is on the latter two parameters to understand the role of shear on the wall pressure

Phase	$n\,(-)$	B (MPa)	$b\,(\mathrm{m^3\,kg^{-1}})$	$q\,(\mathrm{MJ\,kg^{-1}})$	$c\,(\mathrm{J\,(kg\,K)^{-1}})$
Vapour	1.47	0	0	2.1	3610
Liquid	1.19	702.8	6.61×10^{-4}	-1.2	955

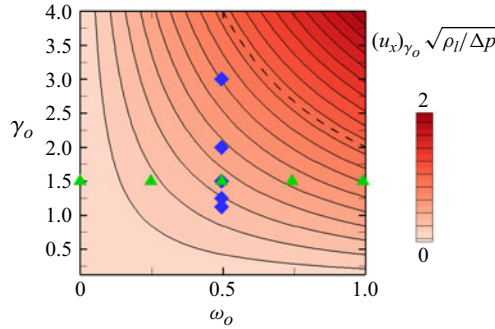Table 1. Constants in the Noble–Abel stiffened-gas equation of state for water.

Figure 2. Initial x-component of the velocity at a distance γ_o from the rigid wall with parameters for the shear rate (▲, green) and initial stand-off distance (◆, blue). Black dashed iso-line (- - -): initial velocity $(u_x)_{\gamma_o}\sqrt{\rho_l/\Delta p} = 1$.

Study	ω_o	γ_o	$p_\infty/\rho_l a_l(\Delta p/\rho_l)^{1/2}$
Baseline	$\dfrac{1}{2}$	$\dfrac{3}{2}$	0.046
ω_o	$\dfrac{1}{4}, \dfrac{1}{2}, \dfrac{3}{4}, 1$	$\dfrac{3}{2}$	—
γ_o	$\dfrac{1}{2}$	$\dfrac{9}{8}, \dfrac{5}{4}, \dfrac{3}{2}, 2, 3$	—
Single wall	0	$\dfrac{9}{8}, \dfrac{5}{4}, \dfrac{3}{2}, 2, 3$	—

Table 2. Initial condition parameters for computations. Parameters are the non-dimensional shear rate, ω_o, and non-dimensional stand-off distance, γ_o, and non-dimensional driving pressure.

produced by bubble collapse with different initial stand-off distances. As a baseline, we consider $\gamma_o = 3/2$ (as done by Yu *et al.* 1995) and $\omega_o = 1/2$. As illustrated in figure 2 and tabulated in table 2, we vary ω_o and γ_o to understand the effect of shear rate and stand-off distances on the wall pressures. While studies conducted by Yu *et al.* (1995) explored $\omega_o \in \{0, 2, 3, 4\}$ for $\Delta p = 50\,\mathrm{kPa}$, in the present study, we focus on lower shear rates at a higher driving pressure. The initial stand-off distances have also been previously investigated for cavitation near a rigid wall (Beig & Johnsen 2015; Dular *et al.* 2019; Gonzalez-Avila *et al.* 2021).

1004 A3-6

3. Results and discussion

3.1. *Overall dynamics*

We first qualitatively describe the role of shear on bubble collapse. Figure 3 shows a time series of pressure contours along the *xz*-centreplane for the baseline case with shear ($\gamma_o = 3/2$ and $\omega_o = 1/2$) and for the case with no mean flow. In the absence of flow, the bubble collapse is axisymmetric as described by Johnsen & Colonius (2009) and Beig (2018). A re-entrant jet directed normal to the wall develops and penetrates the bubble, ultimately impinging upon the bubble interface proximal to the wall at a distance γ_p at time t_p (referred to here as the posterior impingement, and estimated based on pressure contours). The bubble then takes the form of a vortex ring. The water-hammer shock generated by the jet impact propagates radially outward, further collapsing the vortex ring and causing a second shock upon reaching minimum volume at time t_{vc}. In the presence of shear, however, the collapse becomes asymmetric: the bubble rotates in the clockwise direction and adopts an elongated shape due to shear. As a result, the re-entrant jet is initially directed at an angle of approximately $45°$ with respect to the horizontal. As the collapse progresses and the bubble rotates further, the jet trajectory rotates in a manner consistent with observations by Dular *et al.* (2019), such that the jet impinges upon the opposite side of the bubble in a direction nearly parallel to the wall. Compared with the case with no mean flow, this impingement takes place further away from the wall at a distance γ_a and at time t_a such that $t_a < t_p$ (hereafter referred to as the anterior impingement, also estimated based on pressure contours). The water-hammer shock thereby produced further collapses the bubble as it propagates outward. Given the concave shape of the bubble, this shock propagates along the bubble interface before focusing at the farthest end, thereby causing a shock-induced collapse of the gas pocket. This process releases a second water-hammer shock at t_p. Along the shock front, the shock strength is greatest in the direction of propagation of the jet. Eventually, this shock impinges upon the wall. The water-hammer shock produced by a shock-induced collapse originates closer to the wall than in the case with no mean flow. For both, with and without shear, the reflection of shock waves from the neighbouring wall produces weak negative pressure (maximum normalised negative pressure magnitude is 0.02). However, these negative pressures are only observed for an interval $\Delta t/t_c = 0.1$ and, therefore, are not shown for visualisation purposes.

Figure 4 shows the *z*-component of the vorticity along the *xz*-centreplane for the baseline case with shear and for the case with no mean flow. For the case with shear flow, the vorticity of the mean background flow has been subtracted. Without shear flow the vorticity generation is axisymmetric and is localised along the bubble interface. Introducing shear flow results in larger vorticity production, as also observed by Dabiri *et al.* (2010). Further, the vorticity production is asymmetric, with a larger positive ω_z, thereby resulting in a re-entrant jet that is inclined relative to the rigid wall.

The bubble volume at collapse and the location of collapse are important factors governing the wall pressure. Figure 5 shows the time history of the bubble volume and the centroid migration for the baseline case with shear and the case with no shear. The bubble volume in the two cases follows similar behaviour, except that collapse in the shear flow gives rise to a far larger minimum volume and a smaller rebound. In the case with shear, the bubble centroid location increases nearly linearly in the *x*-direction until collapse due to the rotation imparted by the shear. Along the *z*-direction, bubble centroid distance remains nearly unaffected until the bubble collapses. Upon collapse, a smaller bubble centroid migration is observed, i.e. the bubble centroid is farther away from the wall in the case with shear.
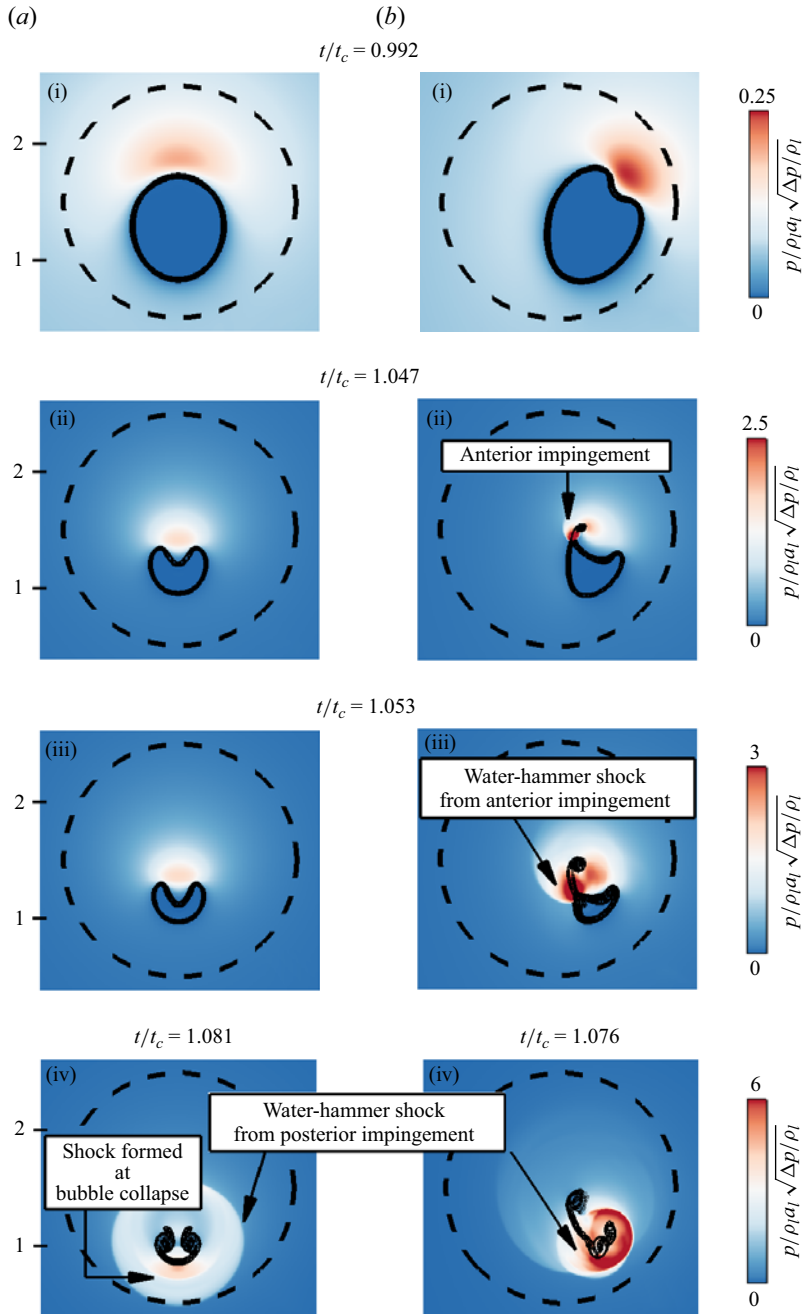
Figure 3. Pressure contours along the *xz*-centreplane of a gas bubble with $\gamma_o = 3/2$ and $p_\infty = 5\,\text{MPa}$ for $\omega_o = 0$ (*a* i–*a* iv) and $1/2$ (*b* i–*b* iv). The dashed line denotes the initial bubble shape. Minimum contour level set to zero for visualisation purposes. Animations for the simulations are given in the supplementary movies available at https://doi.org/10.1017/jfm.2024.1146.

(*a*)　　　　　　　　　　　　(*b*)

$t/t_c = 0.992$

$t/t_c = 1.047$

$t/t_c = 1.053$

$t/t_c = 1.081$　　　　　　$t/t_c = 1.076$
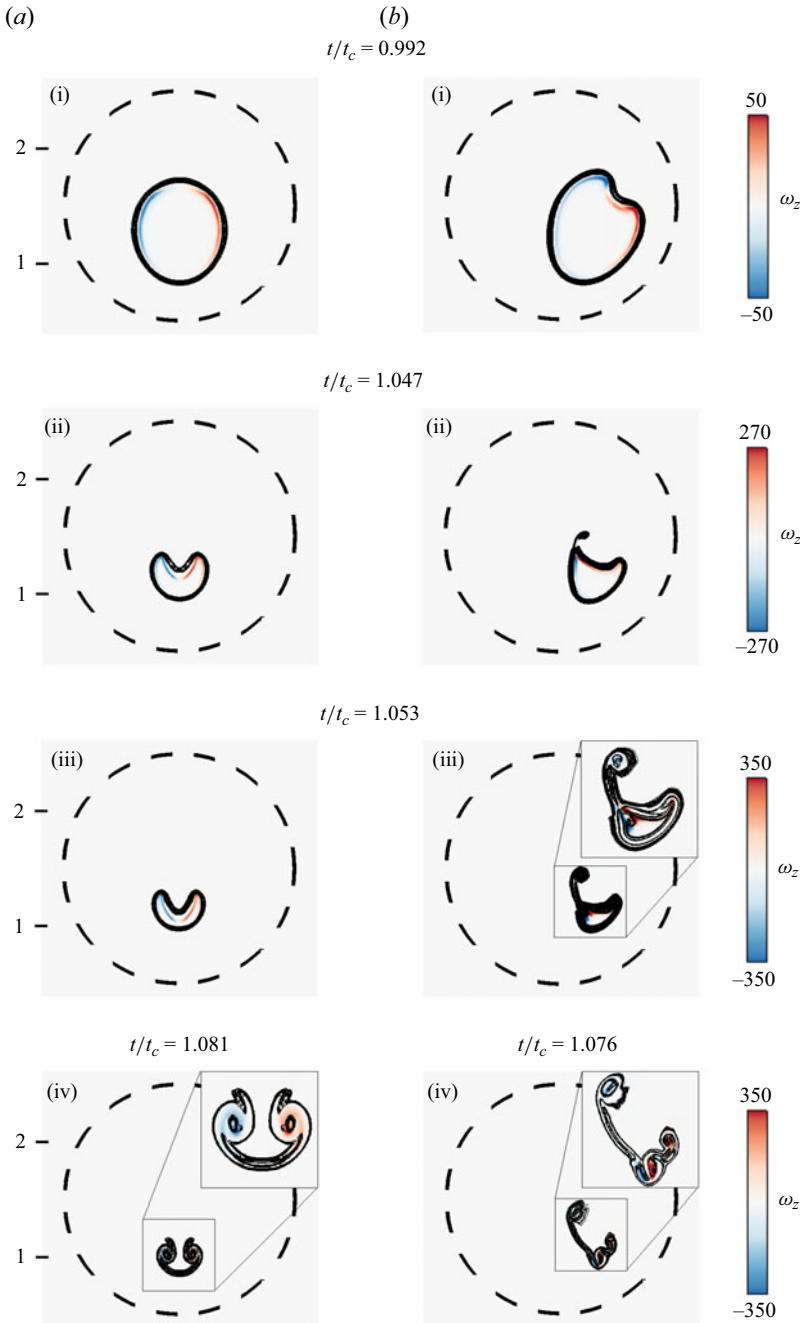
Figure 4. The z-component of the vorticity along the xz-centreplane of a gas bubble with $\gamma_o = 3/2$ and $p_\infty = 5\,\mathrm{MPa}$ for $\omega_o = 0$ (*a* i–*a* iv) and $1/2$ (*b* i–*b* iv). The dashed line denotes the initial bubble shape.

Figure 6 shows the time history of pressure at the wall centre (i.e. x_o location in figure 1) and the maximum wall pressure along with its location. Comparing these two cases, the collapse in a shear flow leads to higher pressures along the wall by approximately 10 %. The anterior shock drives the posterior jet such that the impact of the latter upon the
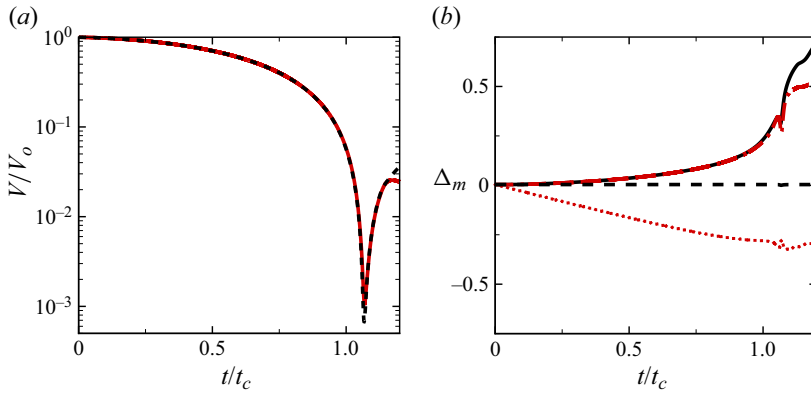
Figure 5. Normalised bubble volume vs time (*a*) with no shear (- - -) and with shear ($\omega_o = 1/2$) (——, red), and centroid migration vs time (*b*) with Δ_z (——, black) and Δ_x (- - -) for the case with no shear and Δ_z (- · -·, red) and Δ_x (······, red) for the case with shear ($\omega_o = 1/2$).
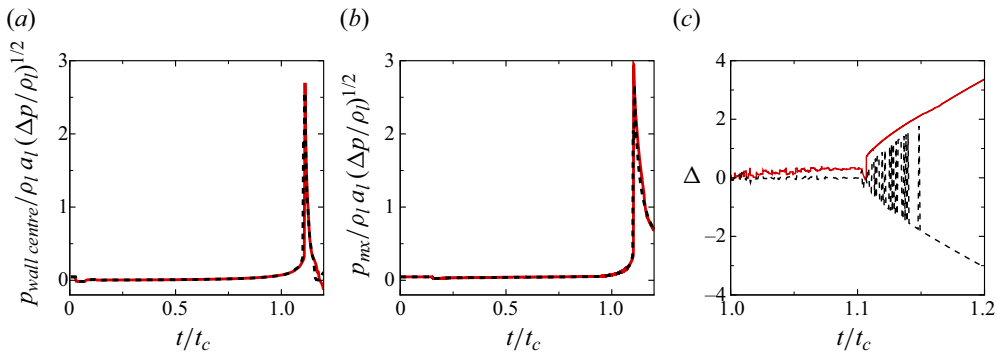

Figure 6. Pressure at the wall centreline ($x = 0$) (*a*), maximum wall pressure (*b*) and its location (*c*) for $\gamma_o = 3/2$, with $\omega_o = 0$ (- - -) and $\omega_o = 1/2$ (——, red).

opposite side of the bubble takes place closer to the wall, thus leading to less shock decay and, therefore, a higher pressure by the time the shock reaches the wall. The normalised location of the maximum pressure is nearly 0.27, downstream in the direction of the shear flow. By contrast, the maximum pressure in collapse in an initially stationary liquid is achieved at the wall centre.

3.2. *Dependence on the shear rate*

To understand how shear affects the bubble dynamics and shock emission, we consider a sequence of simulations with different initial shear rates while holding the initial stand-off distance fixed at $\gamma_o = 3/2$. Figure 7 shows the anterior and posterior impingement migration distances $\Delta = \gamma_i - \gamma_r$, where γ_i is the impingement location and γ_r the reference location (the z-direction reference location for the anterior and posterior migration distances are $\gamma_o + 1$ and $\gamma_o - 1$, respectively), and the pressure produced upon jet impingement. The anterior and posterior impingement locations and times are obtained by finding the maximum pressure in the field contours. Table 3 shows that the time to anterior impingement decreases with increasing shear rate. As reported by Dular *et al.* (2019), the linear translation of the anterior and posterior impingement locations

1004 A3-10
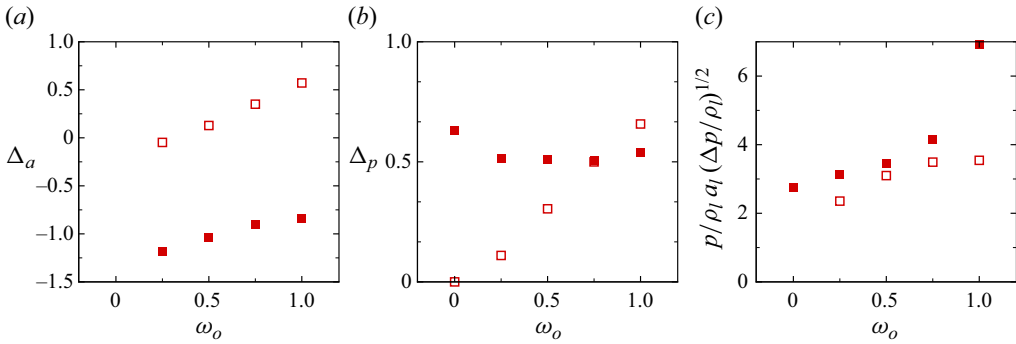
Figure 7. Migration distances of anterior (*a*) Δ_z (■, red), Δ_x (□, red) and posterior (*b*) Δ_z (■, red), Δ_x (□, red) impingement and pressures (*c*) at anterior (□, red) and posterior impingement (■, red) for different shear rates with $\gamma_o = 3/2$.

ω_o	$\dfrac{t_a}{t_c}$ (–)	$\dfrac{t_p}{t_c}$ (–)	$\dfrac{t_{vc}}{t_c}$ (–)	$\Delta t_s = \dfrac{t_p - t_a}{t_c} \times 10^2$ (–)
0	—	1.058	1.066	—
1/4	1.052	1.063	1.064	1.1
1/2	1.047	1.067	1.069	2.0
3/4	1.043	1.069	1.071	2.6
1	1.033	1.074	1.076	4.1

Table 3. Re-entrant jet impingement impact times and minimum volume bubble collapse times for different shear rates, ω_o, with $\gamma_o = 3/2$.

in the *x*-direction are due to the flow. With increasing shear rate, the migration distance along the *z*-direction decreases for anterior impingement. However, the migration distance remains mostly constant along the *z*-direction for posterior impingement. Due to the increasing wall-normal distance of the anterior impingement, the water-hammer shocks travel farther, thus increasing the time to posterior re-entrant jet impingement and bubble collapse. While the wall-normal distance increases for the anterior impingement, the stronger water-hammer shock produced upon impingement produces stronger shocks upon posterior impingement.

Figure 8 shows the bubble collapse volume and centroid migration distance. The bubble rotation due to shear and generation of the two jets and shocks give rise to an asymmetric bubble shape at collapse. Increasing the initial shear rate increases bubble shape asymmetry and results in a larger minimum bubble volume. In the absence of shear, the bubble centroid position is a good approximation to the shock emission location (Rodriguez *et al.* 2022). When shear is present, the overall bubble migration is larger than in the case with no shear due to the migration in the *x*-direction. For all values of $\omega_o > 0$, the bubble centroid migration in the *z*-direction toward the wall is smaller compared with the case with no shear flow.

The maximum pressure and its location are quantities relevant to cavitation damage. Figure 9 shows the maximum wall pressure location and magnitude for different shear rates. We consider the theoretical maximum wall pressure location as the *x*-direction translation of a particle initially located at γ_o, i.e. $(u_x)_{\gamma_o} t_{vc}$. Except $\omega_o = 1/4$, the theoretical location agrees well with the maximum wall pressure location (error ≈ 0.019),
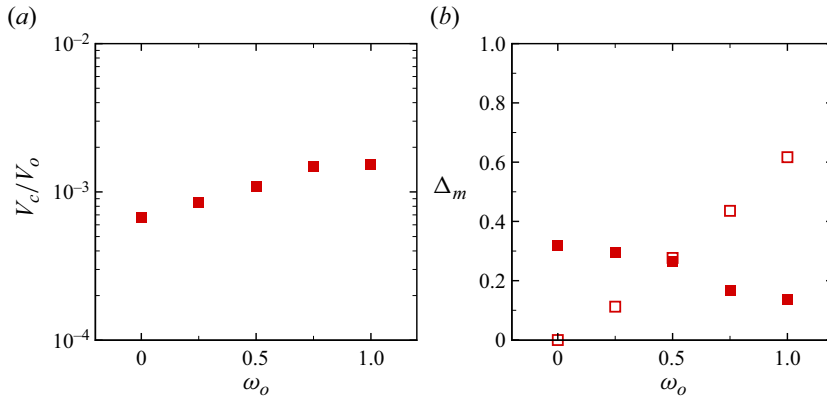
Figure 8. Bubble collapse volume (*a*) and centroid migration distance (*b*) Δ_z ($\blacksquare$, red) and Δ_x ($\square$, red) vs ω_o with $\gamma_o = 3/2$.
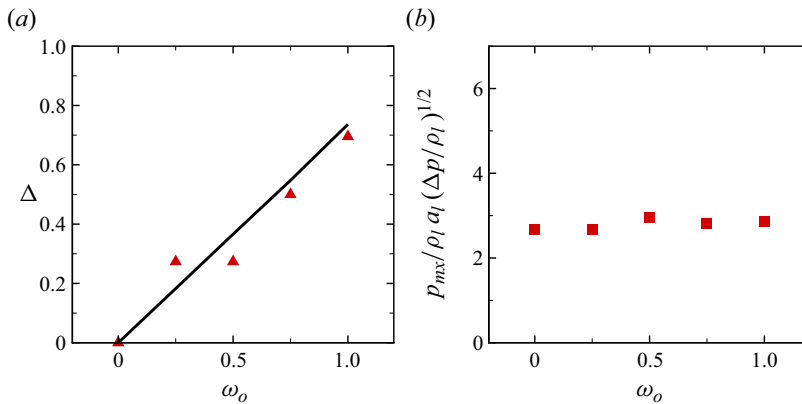

Figure 9. Maximum wall pressure location ($\blacktriangle$, red) and theoretical impact location along the *x*-direction (——) (*a*) and maximum wall pressure (*b*) for $\gamma_o = 3/2$.

underlying the convection effect. The discrepancy is due to the bubble rotation during the collapse and the resulting translation modifying the re-entrant jet trajectory. For $\omega_o = 1/4$ and $1/2$, the shearing and translating bubble achieves the exact maximum pressure location but not the same magnitude. The maximum wall pressure does not significantly vary with the shear rate for this initial stand-off distance. The maximum wall pressure occurs at a non-dimensional shear rate of $1/2$ and is approximately 1.1 times greater than in the case with no shear. Although stronger (posterior) shocks are emitted in the liquid in the cases with shear, the distance travelled to the wall is greater.

3.3. *Dependence on the initial stand-off distance*

As observed earlier, increasing the initial shear rate gives rise to a greater bubble translation and rotation. However, the resulting maximum wall pressures do not significantly vary with the shear rate. Figure 10 shows a time series of pressure contours along the *xz*-centreplane in the case with shear ($\omega_o = 1/2$) for $\gamma_o = 2$ and 3. Increasing the stand-off distance for a fixed shear rate results in the formation of a second jet in a direction that is nearly opposite to that of the anterior jet, forming a pair of converging
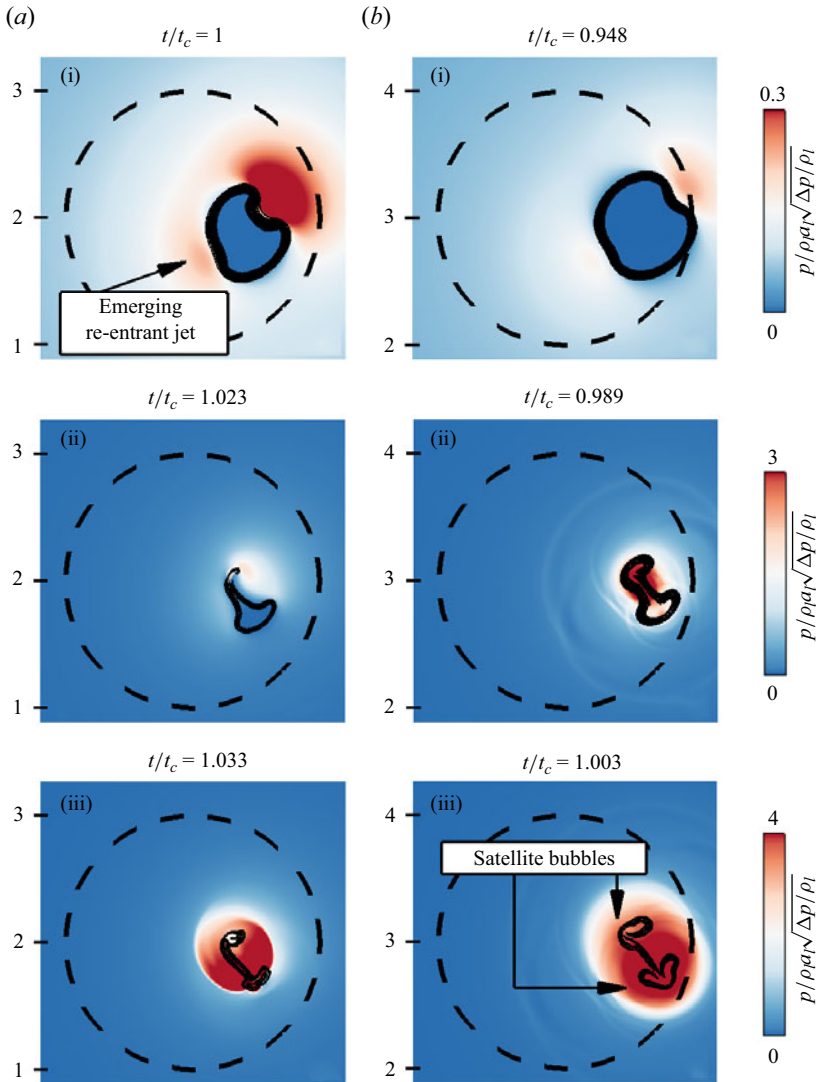
Figure 10. Pressure contours along the xz-centreplane of a gas bubble with $p_\infty = 5\,\text{MPa}$ and $\omega_o = 1/2$ for $\gamma_o = 2$ (a i–a iii) and 3 (b i–b iii). The dashed line denotes the initial bubble shape. Minimum contour level set to zero for visualisation purposes.

jets (see figure 10a i,b i). The axis of convergence of these jets is oblique to the wall, in contrast to the wall-parallel direction seen when a bubble collapses between two plates without any mean flow (Rodriguez *et al.* 2022). Eventually, the two jets impinge upon each other, thereby generating a water-hammer shock (figure 10a ii,b ii) that propagates outward and further collapses the bubble. The remnants of the bubble appear to be similar to the satellite bubbles observed in Dabiri *et al.* (2010) (see figure 10a iii,b iii). For all examined initial stand-off distances, the reflection of the shock from the neighbouring wall produces short-lived weak negative pressures. These negative pressures are not shown for visualisation purposes.

Figure 11 shows the minimum bubble volume and centroid migration distance for different initial stand-off distances. In the absence of shear, Beig (2018) showed that
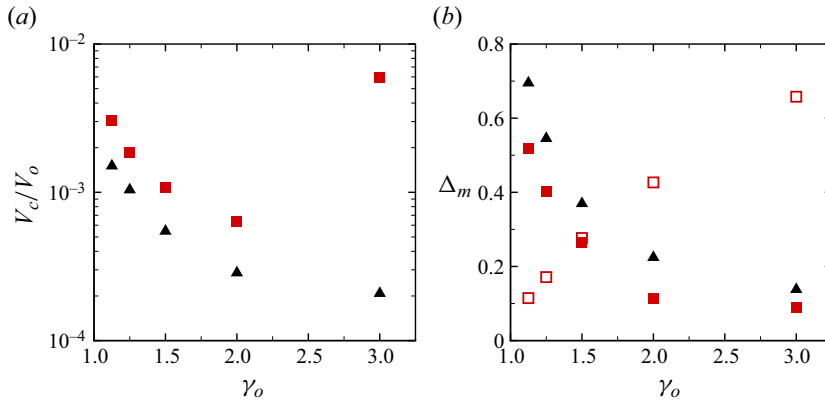
Figure 11. Bubble collapse volume vs stand-off distance (*a*) with no shear flow ($\omega_o = 0$) (▲) and shear flow ($\omega_0 = 1/2$) (■, red), and bubble centroid migration distance vs stand-off distance (*b*) with Δ_z (▲) for the case with no shear and Δ_z (■, red) and Δ_x (□, red) for the case with shear ($\omega_o = 1/2$). Data with no mean shear flow were taken with permission from Rodriguez *et al.* (2022).
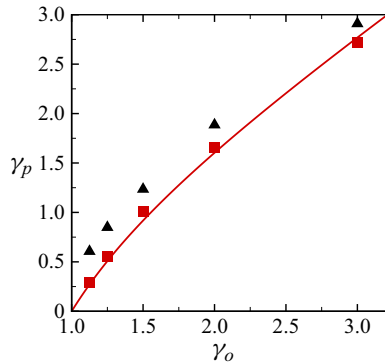

Figure 12. Posterior impingement location along the *z*-direction with no shear flow ($\omega_o = 0$) (▲) and shear flow ($\omega_o = 1/2$) (■, red). Solid red line denotes the relation $\gamma_p = \gamma_o - (\gamma_o^{-4/3})$. For the case with no shear flow, $\gamma_p = \gamma_c$. Data with no mean shear flow were taken with permission from Rodriguez *et al.* (2022).

the minimum bubble volume decreases with increasing initial stand-off distance as the effect of the image bubble decreases and the dynamics of collapse converges to the spherical collapse case, thus leading to greater convergence. With shear, the minimum bubble volume decreases with increasing stand-off distance, except at the highest shear rate. This behaviour is due to the formation of larger satellite bubbles with increasing γ_o (see figure 10). Beyond a critical stand-off distance $\gamma_{o,c} \approx 2$, the collapse morphology is dominated by the formation of converging jets. Increasing the initial stand-off distance in both cases leads to less migration towards the wall.

Figure 12 shows the posterior jet impingement location for different initial stand-off distances and shear rates. In the absence of shear, Rodriguez *et al.* (2022) showed the posterior jet impingement location is nearly equal to the bubble collapse location and can be used to develop scaling relations for the maximum wall pressure. In the case with no shear, the bubble collapse location γ_c is the posterior jet impingement location, i.e. $\gamma_p = \gamma_c$. Additionally, Beig (2018) reported that the bubble collapse location goes as $\gamma_c = \gamma_o - \gamma_o^{-4/3}$. In the presence of shear, the bubble collapse location and
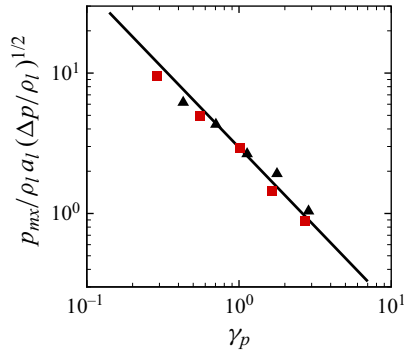
1004 A3-14

Figure 13. Maximum wall pressure vs posterior jet impingement distance with no shear flow ($\omega_o = 0$) (▲) and shear flow ($\omega_o = 1/2$) (■, red). Solid black line (——) slope is -1.13 observed for underwater explosion shocks (Cole 1948). Data with no mean shear flow were taken with permission from Rodriguez *et al.* (2022).

posterior impingement location differ, with the posterior location being closer to the wall. We observe that the same approximation holds and closely matches the jet impingement location. This relationship extends to the maximum wall pressure. Figure 13 shows the maximum wall pressure for different locations of posterior jet impact location. For comparison, we show the maximum wall pressures for cases with no shear from Rodriguez *et al.* (2022). The maximum wall pressures from both cases collapse onto a curve with slope -1.13, representative of underwater explosion shock decay (Cole 1948). For initial stand-off distance $\gamma_o < \gamma_{o,c}$, the maximum wall pressure obtained in the case with shear is higher. However, lower wall pressures are obtained as the effect of the image bubble reduces and the collapse becomes shear dominated. The scaling relation can be used to estimate the maximum wall pressure for a location of posterior jet impingement.

4. Conclusions

Numerical simulations are conducted to determine the role of a mean shear on the inertial collapse of a gas bubble near a rigid surface. Shear breaks the symmetry of the collapse by causing migration in the streamwise direction and rotation. As a result, the re-entrant jet originating from the bubble end farthest from the wall rotates and impinges the opposite side of the bubble in a direction that is not normal to the wall. The resulting water-hammer shock propagates outward and causes a second shock-induced collapse of the part of the bubble closest to the wall. Although the pressure thereby generated increases with increasing shear, the maximum wall pressure only increases marginally. The shock is strongest in the direction of motion of the jet, such that that portion of the shock travels a longer distance before impinging the wall, thus decaying more than the portion of the shock travelling the shortest distance to the wall. As a result, the wall pressures are only marginally higher in collapse with shear for a non-dimensional shear rate of $1/2$. Even in the presence of shear, the dependence of the wall pressure on the stand-off distance obeys previously determined scalings corresponding to bubble collapse in an initially stationary fluid near a wall. For a critical initial stand-off distance $\gamma_{o,c} > 2$ where the effect of the image bubble is reduced and the collapse becomes shear dominated, the maximum wall pressure becomes lower compared with the case with no shear flow.

While this study has yielded valuable insights into the effects of shear and initial stand-off distance on the bubble collapse dynamics, several avenues for future research remain. Future investigations could incorporate the bubble growth phase to provide a

more comprehensive understanding of the entire bubble lifecycle under shear. This would include vapour condensation and surface tension effect during bubble growth under shear flow and varying initial stand-off distances. Additionally, studying quantities such as wall shear stress and temperatures would offer deeper insights into surface cleaning and material damage in the presence of mean shear flow (Dijkink & Ohl 2008; Beig *et al.* 2018; Zeng *et al.* 2018; Kondo & Ando 2019).

Author ORCIDs.

Sahil Bhola https://orcid.org/0000-0002-3676-6302;

Mauro Rodriguez Jr. https://orcid.org/0000-0003-0545-0265;

Shahaboddin A. Beig https://orcid.org/0000-0002-6865-4858;

Charlotte N. Barbier https://orcid.org/0000-0003-2752-0148;

Eric Johnsen https://orcid.org/0000-0001-9530-408X.

REFERENCES

ALLAIRE, G., CLERC, S. & KOKH, S. 2002 A five-equation model for the simulation of interfaces between compressible fluids. *J. Comput. Phys.* **181**, 577–616.

ANDO, K., SUGAWARA, M. & SAKOTA, R. 2021 Particle removal in ultrasonic water flow cleaning role of cavitation bubbles as cleaning agents. *Solid State Phenom.* **314**, 218–221.

BEIG, S.A. 2018 A computational study of the inertial collapse of gas bubbles near a rigid surface. PhD thesis, University of Michigan, Ann Arbor, MI.

BEIG, S.A., ABOULHASANZADEH, B. & JOHNSEN, E. 2018 Temperatures produced by inertially collapsing bubbles near rigid surfaces. *J. Fluid Mech.* **852**, 105–125.

BEIG, S.A. & JOHNSEN, E. 2015 Maintaining interface equilibrium conditions in compressible multiphase flows using interface capturing. *J. Comput. Phys.* **302**, 548–566.

BENJAMIN, T.B. & ELLIS, A.T. 1966 The collapse of cavitation bubbles and the pressures thereby produced against solid boundaries. *Phil. Trans. R. Soc.* A **260**, 221–240.

BIDI, S., SHAMS, A., KOUKOUVINIS, P. & GAVAISES, M. 2023 Prediction of shock heating during ultrasound-induced bubble collapse using real-fluid equations of state. *Ultrason. Sonochem.* **101**, 106663.

BLAKE, J.R. & GIBSON, D.C. 1987 Cavitation bubbles near boundaries. *Annu. Rev. Fluid Mech.* **19**, 99–123.

BRIJKISHORE, KHARE, R. & PRASAD, V. 2021 Prediction of cavitation and its mitigation techniques in hydraulic turbines – a review. *Ocean Engng* **221**, 108512.

BRUJAN, E.A., KEEN, G.S., VOGEL, A. & BLAKE, J.R. 2002 The final stage of the collapse of a cavitation bubble close to a rigid boundary. *Phys. Fluids* **14**, 85–92.

BUSSMANN, A., RIAHI, F., GÖKCE, B., ADAMI, S., BARCIKOWSKI, S. & ADAMS, N.A. 2023 Investigation of cavitation bubble dynamics near a solid wall by high-resolution numerical simulation. *Phys. Fluids* **35** (1), 016115.

CECCIO, S.L. & BRENNEN, C.E. 1991 Observations of the dynamics and acoustics of travelling bubble cavitation. *J. Fluid Mech.* **233**, 633–660.

CHAVES, H., KNAPP, M., KUBITZEK, A., OBERMEIER, F. & SCHNEIDER, T. 1995 Experimental study of cavitation in the nozzle hole of diesel injectors using transparent nozzles. *SAE Trans.* **104**, 645–657.

CHEN, X. 2010 Simulation of 2D cavitation bubble growth under shear flow by lattice Boltzmann model. *Commun. Comput. Phys.* **7**, 212–223.

COLE, R.H. 1948 *Underwater Explosions*. Princeton University Press.

CORALIC, V. & COLONIUS, T. 2013 Shock-induced collapse of a bubble inside a deformable vessel. *Eur. J. Mech. (B/Fluids)* **40**, 64–74.

DABIRI, S., SIRIGNANO, W.A. & JOSEPH, D.D. 2010 Interaction between a cavitation bubble and shear flow. *J. Fluid Mech.* **651**, 93–116.

DE CHIZELLE, Y.K., CECCIO, S.L. & BRENNEN, C.E. 1995 Observations and scaling of travelling bubble cavitation. *J. Fluid Mech.* **293**, 99–126.

DIJKINK, R. & OHL, C.-D. 2008 Measurement of cavitation induced wall shear stress. *Appl. Phys. Lett.* **93** (25), 254107.

DULAR, M., POŽAR, T., ZEVNIK, J. & PETKOVŠEK, R. 2019 High speed observation of damage created by a collapse of a single cavitation bubble. *Wear* **418**, 13–23.

ESCALER, X., EGUSQUIZA, E., FARHAT, M., AVELLAN, F. & COUSSIRAT, M. 2006 Detection of cavitation in hydraulic turbines. *Mech. Syst. Signal Process* **20** (4), 983–1007.

FRANC, J.-P., RIONDET, M., KARIMI, A. & CHAHINE, G.L. 2011 Impact load measurements in an erosive cavitating flow. *Trans. ASME J. Fluids Engng* **133**, 1–8.

GAVAISES, M., PAPOULIAS, D., ANDRIOTIS, A., GIANNADAKIS, E. & THEODORAKAKOS, A. 2007 Link between cavitation development and erosion damage in diesel injector nozzles. *Tech. Rep.* SAE Technical Paper 2007-01-0246.

GIANNADAKIS, E., GAVAISES, M. & ARCOUMANIS, C. 2008 Modelling of cavitation in diesel injector nozzles. *J. Fluid Mech.* **616**, 153–193.

GIBSON, D.C. 1968 Cavitation adjacent to plane boundaries. In *Proc. 3rd Australasian Conf. on Hydraulics and Fluid Mechanics, Sydney*, pp. 210–214.

GONZALEZ-AVILA, S.R., DENNER, F. & OHL, C.D. 2021 The acoustic pressure generated by the cavitation bubble expansion and collapse near a rigid wall. *Phys. Fluids* **33**, 032118.

HAINES, J.R., MCMANAMY, T.J., GABRIEL, T.A., BATTLE, R.E., CHIPLEY, K.K., CRABTREE, J.A., JACOBS, L.L., LOUSTEAU, D.C., RENNICH, M.J. & RIEMER, B.W. 2014 Spallation neutron source target station design, development, and commissioning. *Nucl. Instrum. Meth. Phys. Res.* A **764**, 94–115.

HICKLING, R. & PLESSET, M.S. 1964 Collapse and rebound of a spherical bubble in water. *Phys. Fluids* **7**, 7–14.

JOHNSEN, E. & COLONIUS, T. 2009 Numerical simulations of non-spherical bubble collapse. *J. Fluid Mech.* **629**, 231–262.

KAPILA, A.K., MENIKOFF, R., BDZIL, J.B., SON, S.F. & STEWART, D.S. 2001 Two-phase modeling of deflagration-to-detonation transition in granular materials: reduced equations. *Phys. Fluids* **13**, 3002–3024.

KIM, K.H., CHAHINE, G., FRANC, J.P. & KARIMI, A. (ed.) 2014 *Advanced Experimental and Numerical Techniques for Cavitation Erosion Prediction*, Fluid Mechanics and its Applications, vol. 106. Springer.

KIM, W., KIM, T.H., CHOI, J. & KIM, H.Y. 2009 Mechanism of particle removal by megasonic waves. *Appl. Phys. Lett.* **94** (8), 081908.

KONDO, T. & ANDO, K. 2019 Simulation of high-speed droplet impact against a dry/wet rigid wall for understanding the mechanism of liquid jet cleaning. *Phys. Fluids* **31** (1), 013303.

LAUTERBORN, W. & BOLLE, H. 1975 Experimental investigations of cavitation-bubble collapse in the neighbourhood of a solid boundary. *J. Fluid Mech.* **72**, 391.

LAUTERBORN, W., LECHNER, C., KOCH, M. & METTIN, R. 2018 Bubble models and real bubbles: Rayleigh and energy-deposit cases in a tait-compressible liquid. *IMA J. Applied Maths* **83** (4), 556–589.

LE MÉTAYER, O. & SAUREL, R. 2016 The Noble–Abel stiffened-gas equation of state. *Phys. Fluids* **28**, 1–22.

LINDAU, O. & LAUTERBORN, W. 2003 Cinematographic observation of the collapse and rebound of a laser-produced cavitation bubble near a wall. *J. Fluid Mech.* **479**, 327–348.

MURRONE, A. & GUILLARD, H. 2005 A five equation reduced model for compressible two phase flow problems. *J. Comput. Phys.* **202**, 664–698.

NAUDÉ, C.F. & ELLIS, A.T. 1961 On the mechanism of cavitation damage by nonhemispherical cavities collapsing in contact with a solid boundary. *Trans. ASME J. Basic Engng* **83**, 648–656.

PATELLA, R.F., ARCHER, A. & FLAGEUL, C. 2012 Numerical and experimental investigations on cavitation erosion. In *IOP Conference Series: Earth and Environmental Science*, vol. 15, p. 022013. IOP Publishing.

PERIGAUD, G. & SAUREL, R. 2005 A compressible flow model with capillary effects. *J. Comput. Phys.* **209**, 139–178.

PETITPAS, F., MASSONI, J., SAUREL, R., LAPEBIE, E. & MUNIER, L. 2009 Diffuse interface model for high speed cavitating underwater systems. *Intl J. Multiphase Flow* **35** (8), 747–759.

PHILIPP, A. & LAUTERBORN, W. 1998 Cavitation erosion by single laser-produced bubbles. *J. Fluid Mech.* **361**, 75–116.

PLESSET, M.S. 1949 The dynamics of cavitation bubbles. *J. Appl. Mech.* **16**, 277–282.

PLESSET, M.S. & CHAPMAN, R.B. 1971 Collapse of an initially spherical vapour cavity in the neighbourhood of a solid boundary. *J. Fluid Mech.* **47**, 283–290.

PRESTON, A.T. 2004 Modeling heat and mass transfer in bubbly cavitating flows and shock waves in cavitating nozzles. PhD thesis, California Institute of Technology, Padasena, CA.

RAYLEIGH, LORD 1917 On the pressure developed in a liquid during the collapse of a spherical cavity. *Phil. Mag.* **34**, 94–98.

RIEMER, B.W., MCCLINTOCK, D.A., KAMINSKAS, S. & ABDOU, A.A. 2014 Correlation between simulations and cavitation-induced erosion damage in spallation neutron source target modules after operation. *J. Nucl. Mater.* **450**, 183–191.

RODRIGUEZ, M., BEIG, S.A., BARBIER, C.N. & JOHNSEN, E. 2022 Dynamics of an inertially collapsing gas bubble between two parallel, rigid walls. *J. Fluid Mech.* **946**, A43.

SHCHUKIN, D.G., SKORB, E., BELOVA, V. & MÖHWALD, H. 2011 Ultrasonic cavitation at solid surfaces. *Adv. Mater.* **23** (17), 1922–1934.

SHIMA, A., TOMITA, Y. & TAKAHASHI, K. 1984 The collapse of a gas bubble near a solid wall by a shock wave and the induced impulsive pressure. *Proc. Inst. Mech. Engrs* C **198**, 81–86.

SHUTLER, N.D. & MESLER, R.B. 1965 A photographic study of the dynamics and damage capabilities of bubbles collapsing near solid boundaries. *Trans. ASME J. Basic Engng* **87**, 511–517.

STOREY, B.D. & SZERI, A.J. 2000 A reduced model of cavitation physics for use in sonochemistry. *J. Acoust. Soc. Am.* **107**, 2866.

SUPPONEN, O., OBRESCHKOW, D., KOBEL, P., TINGUELY, M., DORSAZ, N. & FARHAT, M. 2017 Shock waves from nonspherical cavitation bubbles. *Phys. Rev. Fluids* **2**, 1–20.

SUPPONEN, O., OBRESCHKOW, D., TINGUELY, M., KOBEL, P., DORSAZ, N. & FARHAT, M. 2016 Scaling laws for jets of single cavitation bubbles. *J. Fluid Mech.* **802**, 263–293.

THOMPSON, K.W. 1990 Time-dependent boundary conditions for hyperbolic systems, II. *J. Comput. Phys.* **89**, 439–461.

TIWARI, A., PANTANO, C. & FREUND, J.B. 2015 Growth-and-collapse dynamics of small bubble clusters near a wall. *J. Fluid Mech.* **775**, 1–23.

TRUMMLER, T., BRYNGELSON, S.H., SCHMIDMAYER, K., SCHMIDT, S.J., COLONIUS, T. & ADAMS, N.A. 2020 Near-surface dynamics of a gas bubble collapsing above a crevice. *J. Fluid Mech.* **899**, 1–21.

VENNING, J.A., PEARCE, B.W. & BRANDNER, P.A. 2022 Nucleation effects on cloud cavitation about a hydrofoil. *J. Fluid Mech.* **947**, A1.

WHITE, W., BEIG, S.A. & JOHNSEN, E. 2023 Pressure fields produced by single-bubble collapse near a corner. *Phys. Rev. Fluids* **8**, 023601.

WINDER, D., LIN, L. & MACH, J. 2021 Incorporating bubble growth volume feedback to improve simulation of the response of a structure containing liquid and gas to sudden energy input. *Nucl. Instrum. Meth. Phys. Res.* A **1005**, 165371.

YANG, X., LIU, C., LI, J., ZHAO, M. & HU, C. 2023 Implosion of a bubble pair near a solid surface. *Phys. Rev. Fluids* **8** (2), 023602.

YANG, X., LIU, C., WAN, D. & HU, C. 2021 Numerical study of the shock wave and pressure induced by single bubble collapse near planar solid wall. *Phys. Fluids* **33** (7), 073311.

YU, P.W., CECCIO, S.L. & TRYGGVASON, G. 1995 The collapse of a cavitation bubble in shear flows – a numerical study. *Phys. Fluids* **7**, 2608–2616.

ZENG, Q., GONZALEZ-AVILA, S.R., DIJKINK, R., KOUKOUVINIS, P., GAVAISES, M. & OHL, C.-D. 2018 Wall shear stress from jetting cavitation bubbles. *J. Fluid Mech.* **846**, 341–355.